

RESEARCH ARTICLE

10.1029/2018JB016271

Key Points:

- High-resolution teleseismic double-difference tomography shifts earthquakes tens of kilometers southwest along the Ecuador seismogenic zone
- The revised catalog (1961-2016, $M > 3$) better models InSAR data and confirms persistent megathrust segmentation over seismic cycles
- The 2016 $M_{6.7}$ and $M_{6.9}$ aftershocks of the $M_{7.8}$ Pedernales event ruptured northeast of the mainshock in areas of moderate to high coupling

Supporting Information:

- Supporting Information S1

Correspondence to:

K. B. Kwong,
kkwong@smu.edu

Citation:





Kwong, K. B., DeShon, H. R., Kim, J. W., & Lu, Z. (2019). Resolving teleseismic earthquake catalog and InSAR data discrepancies in absolute space to explore rupture complexity along the Ecuadorian megathrust fault. *Journal of Geophysical Research: Solid Earth*, 124. <https://doi.org/10.1029/2018JB016271>

Received 24 JUN 2018

Accepted 18 JUN 2019

Accepted article online 24 JUN 2019

Resolving Teleseismic Earthquake Catalog and InSAR Data Discrepancies in Absolute Space to Explore Rupture Complexity Along the Ecuadorian Megathrust Fault

Kevin B. Kwong¹ , Heather R. DeShon¹ , Jin Woo Kim¹ , and Zhong Lu¹ 

¹Department of Earth Sciences, Southern Methodist University, Dallas, TX, USA

Abstract The 2016 M_W 7.8 Pedernales, Ecuador, megathrust earthquake produced notable crustal deformation and generated an extensive aftershock sequence that included two $M_{6.5+}$ events. We combine an improved teleseismic earthquake catalog for Ecuador with analysis of coseismic interferometric synthetic aperture radar data derived from the Sentinel-1A satellite to better delineate the spatial and temporal slip history of the megathrust fault in absolute space. The revised teleseismic catalog spans 1961-2016 and incorporates catalog phase onset times and waveform correlation derived differential times to locate earthquakes. Using teleseismic double-difference (DD) tomography to simultaneously solve for an updated regional 3-D compressional velocity model and locations yields earthquakes shifted ~25 km southwest relative to rapidly available teleseismic catalogs. The DD catalog better compares in absolute space to the Ecuadorian local catalog and better models the measured deformation fields of the 2016 Pedernales mainshock and largest aftershocks. Additionally, the DD mainshock location agrees with local-scale seismic and geodetic studies that show the 2016 event had concentrated slip on a highly coupled asperity that likely participated in the 1942 Ecuador megathrust earthquake. The two large aftershocks also ruptured on the megathrust where moderate to strong interseismic coupling is observed. The DD catalog contains moderate-sized aftershocks that concentrate outside high slip regions, primarily in areas that produced earthquakes during the interseismic cycle, and outside areas of aseismic slip. Development of rapid relative location approaches linking new seismicity to better constrained global catalogs could aid with near real-time hazard assessment in areas lacking local data.

1. Introduction

Studies of megathrust earthquakes along the Columbia-Ecuador subduction zone were influential to derive the asperity model for rupture heterogeneity (e.g., Kanamori and McNally, 1982; Lay et al., 1982), here defined as the location of increased strength and high stress on a fault that in turn produces the largest slip during an earthquake. Modern geodetic models confirm the presence of a heterogeneous fault with discrete areas of high coupling, interpreted as asperities frictionally locked and accumulating strain, surrounded by areas with variable coupling (e.g., Moreno et al., 2014). Geodetic data from Ecuador establish a subduction plate interface with several large asperities (Chlieh et al., 2014; Nocquet et al., 2014, 2017) surrounded by areas of aseismic slip (Rolandone et al., 2018; Vaca et al., 2018; Vallée et al., 2013). Variable resolution between geodetic and seismic data sets of megathrust faults, which lie largely offshore, continues to limit efforts to map and compare coupling and high slip. Geodetic and seismic slip modeling requires a known geometry for the subducting slab, which in turn is frequently constrained by teleseismic and regional- to local-scale earthquake catalogs. The catalogs can exhibit tens of kilometers spatial bias, especially in depth, due to incorrectly modeled velocity structure (e.g., Engdahl et al., 1998, and references therein). The Columbia-Ecuador subduction zone now provides key data sets to resolve these issues due to the growing availability of far-field and near-field seismic and geodetic sensors deployed prior to and following the 2016 M_W 7.8 Pedernales earthquakes. Combined, the data provide improved resolution to image spatial discrepancies in the teleseismic and satellite geodetic data sets, with independent local seismic data for verification.

Subduction of the Nazca plate below Ecuador has generated a history of large to great earthquakes, and the 16 April 2016 M_W 7.8 Pedernales earthquake is the most recent (Figure 1). The largest, the 1906 M_W 8.8

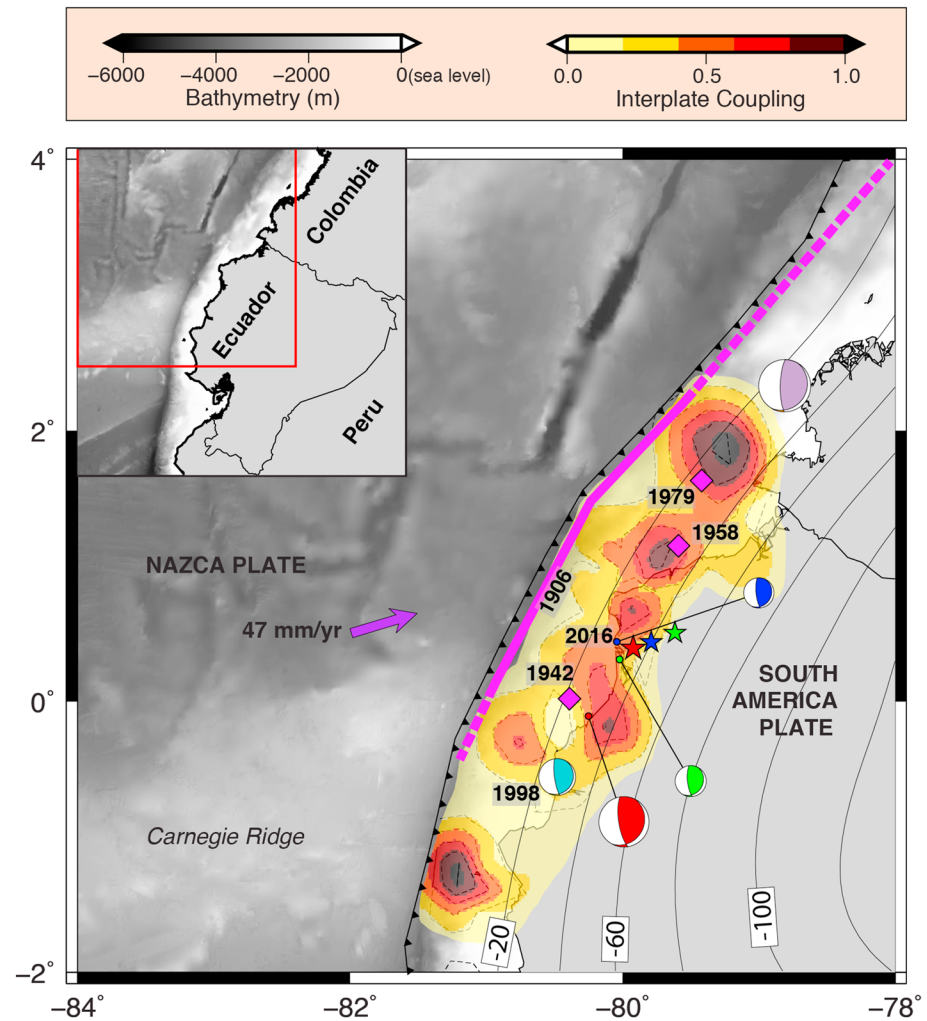


Figure 1. Ecuador-Columbia subduction zone marks subduction of the Nazca plate under the northern part of South America (inset). Main map: Along Ecuador, the Carnegie Ridge and inactive spreading center structures subduct obliquely where the Nazca plate subducts under South America at a rate of ~ 47 mm/year. The magenta indicates historic large earthquakes (magenta diamonds and lines; Mendoza & Dewey, 1984), inferred rupture length of the 1906 earthquake (solid magenta line; Yoshimoto et al., 2017), and alternative maximum rupture lengths from earlier studies (dashed magenta line). Recent earthquakes with Global Centroid Moment Tensor solutions (beachballs) and U.S. Geological Survey reported epicenter (stars) follows color coding: 1998 M_W 7.1 (teal), 1979 M_W 8.2 (purple), 2016 M_W 7.8 mainshock (red), M_W 6.7 aftershock (blue), and M_W 6.9 aftershock (green). Interseismic plate coupling model is from Chlieh et al. (2014). The contour lines for the Slab2.0 model (Hayes, 2018) are in 20-km intervals with negative numbers indicating depth to top of slab.

earthquake, likely ruptured all or most of the megathrust fault (~ 500 km; Kanamori & McNally, 1982; Kelleher, 1972). Subsequent smaller events (1942 M_W 7.8, 1958 M_W 7.7, 1979 M_W 8.2, and 1998 M_W 7.1) are thought to have ruptured several discrete asperities within the 1906 slip area based primarily on aftershock locations and coseismic slip models (e.g., Kanamori & McNally, 1982; Mendoza & Dewey, 1984; Ye et al., 2016), although a recent slip model of the 1906 event suggests that it did not overlap with the later earthquakes (Yoshimoto et al., 2017; Figure 1). The 2016 Pedernales event occurred on the northern edge of the subducting Carnegie Ridge and the 1942 earthquake. Here the subduction rate is ~ 47 mm/year (Nazca Plate with respect to the North Andean Silver) and the convergence direction is slightly oblique to trench strike (Chen et al., 2001; Nocquet et al., 2014, 2017; Yepes et al., 2016; Figure 1). Whether the 2016 rupture overlapped with the 1942 event has been discussed in several studies (He et al., 2017; Nocquet et al., 2017; Ye et al., 2016; Yi et al., 2018; Yoshimoto et al., 2017) but remains a point of scientific debate.

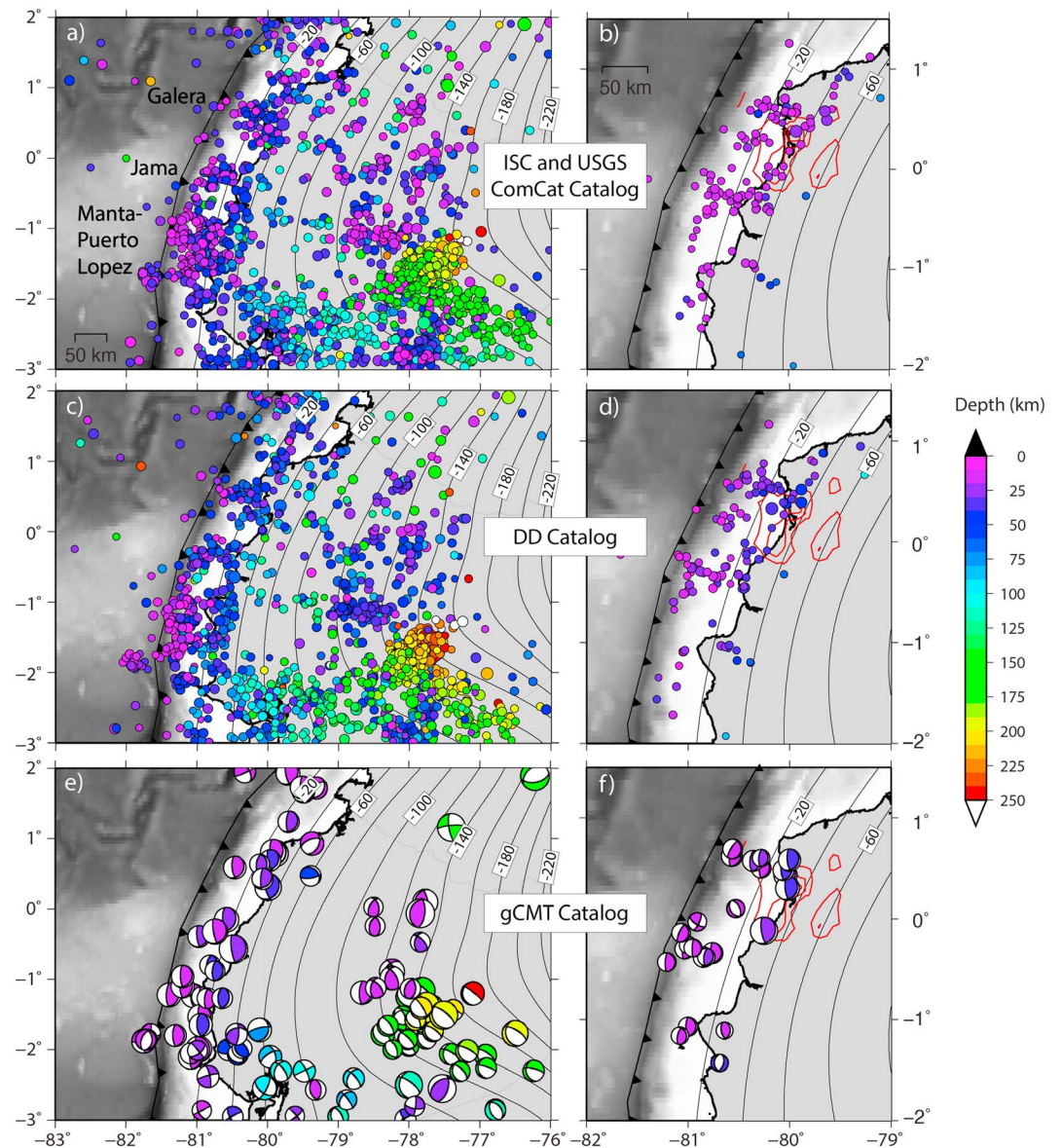


Figure 2. Earthquake and centroid catalogs from 1961 through 15 April 2016 (left column: a, c, and e) and from 16 April through 31 December 2016 (right column: b, d, and f). Top row: the combined International Seismological Centre (ISC) and Comprehensive Catalog (ComCat) catalog; Middle row: double-difference (DD) relocations (this study); Bottom row: Global Centroid Moment Tensor solutions. Color coding indicates depth. Contour interval for the Slab2.0 model (Hayes, 2018) follows Figure 1. Right column also shows the slip contours (red at 1-m intervals) for the 2016 M_W 7.8 earthquake (earthquakes.usgs.gov, 2016) for reference.

Along the Ecuador-Columbia subduction zone, interplate seismicity, positive Bouguer anomalies, and marine terraces spatially correspond to areas with significant or high plate coupling, resulting in a highly segmented margin (Font et al., 2013; Gutscher et al., 1999). Different scales of bathymetrically high features entering the trench along Ecuador, such as the large Carnegie Ridge and smaller seamounts, produce variable plate coupling reflected in the geodetic interseismic coupling models (Chlieh et al., 2014; Collot et al., 2017; Nocquet et al., 2017; Figure 1) and mapping of aseismic slip (Nocquet et al., 2017; Rolandone et al., 2018; Vaca et al., 2018). From -2° S to 1° N, the megathrust fault has been divided into three distinctive regions (Figure 2). The Galera alignment is an active region of seismicity that trends perpendicular to the trench; the 2016 Pedernales epicenter lies within or at the edge of this segment (Figure 2b). The Jama and Manta Puerto Lopez segments are associated with two regions of strongly

clustered seismicity on the subducted Carnegie Ridge. Seamount subduction occurs between the Galera and Jama seismic region, in an area interpreted as weakly coupled and relatively aseismic (Marcaillou et al., 2016). Subducted physical features such as seamounts and ridges, changes in age and thermal profile of the upper or lower plate, and variable changes in composition or thickness of incoming sediments have been used to explain heterogeneity along the South America subduction zone (Bilek, 2010), but improved earthquake locations in absolute space are required to fully map seismogenic variability along Ecuador (e.g., El Hariri et al., 2013).

We relocate teleseismic events along the Ecuador subduction zone region with two goals: (1) to constrain shallow subduction zone processes using improved hypocenters prior to and after the Pedernales mainshock and interferometric synthetic aperture radar (InSAR) derived deformation models and (2) to show how teleseismic double-difference (DD) tomography links phase data from different catalogs to remove spatial bias in global hypocenters. Here we jointly solve for teleseismic relocations and a regional compressional 3-D velocity model embedded within a static global 3-D velocity model to better account for the strongly varying velocity field associated with the subducting Nazca lithosphere. The reviewed International Seismological Centre (ISC) Bulletin combined with the U.S. Geological Survey (USGS) Advanced National Seismic System (ANSS) Comprehensive Catalog (ComCat) spanning from 1961 to 2016 (Figures 2a and 2b) provides the earthquake data. The ComCat includes rapid analysis and distribution of phase data for significant earthquakes, and we link ComCat to the comprehensive reviewed ISC catalog via phase differential times. We observe and model coseismic InSAR images of the 2016 M_w 7.8 mainshock, the large M_w 6.7, and the 6.9 aftershocks on 18 May 2016 (hereafter, aftershock 1 and aftershock 2, respectively) to provide spatial information of surface deformation during the sequence and confirm DD relocation results. We compare the DD catalog paired with the InSAR coseismic images (Sentinel-1A repeat interval of 12 days) with interseismic coupling models (Chlieh et al., 2014; Nocquet et al., 2017) to identify persistent and/or new asperities along the megathrust. The relationship between spatial patterns of coseismic slip, aftershock locations, interseismic plate coupling, and aseismic slip models provide important assessment of the long-term earthquake and tsunami hazard of this margin.

2. Methods and Data

2.1. Earthquake Catalogs

Global- and country-wide earthquake catalogs report seismic activity in Ecuador, and each data set provides unique hypocenters, uncertainties, magnitudes, and number of events calculated through global or regional 1-D velocity models. The ISC Bulletin, the ANSS ComCat, and the Global Centroid Moment Tensor (gCMT) catalogs provide easily accessed hypocenter and moment tensor solutions. The ISC is the most complete global collection of local through teleseismic phase onset times, including depth phases, and associated hypocenters with magnitudes. The ISC also provides a relocated, reduced uncertainty catalog called the reviewed ISC Bulletin derived using the EHB method (Engdahl et al., 1998). The reviewed Bulletin is generally published 2 years in arrears (Bondár & Storchak, 2011), however, making it difficult to study mainshock-aftershock sequences in near real time. In contrast, rapid publication of phase data used by the USGS National Earthquake Information Center and published in the ANSS ComCat allows real-time analysis but contains only primary first arrivals and no depth phases. In both catalogs, location procedures use global 1-D velocity models (ak135 for the revised ISC bulletin and iasp91 for the ComCat). Significant spatial biases on the order of tens of kilometers in epicenter and depth have been shown to result from unmodeled structure within subduction zones (e.g., Engdahl et al., 1998; Storchak et al., 2000; Syracuse & Abers, 2009, and references therein). Additionally, teleseismic earthquake catalogs can have hypocenters shifted toward dense network coverage, such as toward land networks for offshore subduction-related events, and the natural trade-off between depth and origin time in the inverse solution can result in significant depth uncertainty, especially when depth phase times are not available. For the relocation study of the Ecuador-Columbia margin, we link the reviewed ISC and rapid ComCat phase catalog data via differential times, and when available, correlated waveforms extracted from the Incorporated Research Institutions for Seismology Data Management Center (IRIS DMC) allow us to produce higher-accuracy differential time measurements. For initial hypocenters, the reviewed ISC bulletin takes precedence over the ComCat; the transition between catalogs takes place in late 2013 for our data set.

Table 1
Comparing Event Locations of the 16 April 2016 Mainshock and 18 May Aftershocks Between Catalogs

Catalog	Origin time (UTC)	Latitude (°N)	Longitude (°W)	Depth (km)
Mainshock (Mw 7.8, 16 April 2016)				
USGS ComCat	23:58:36.98	0.38	79.92	20.6
DD Relocation	23:58:34.92	0.33	80.17	35.8
IG-EPN	23:58:34.31	0.31	80.12	17.4
Nocquet et al. (2017)	23:58:33.00	0.35	80.17	17.0
gCMT Centroid	23:58:57.00	0.12	80.25	22.3
Aftershock 1 (Mw 6.7, 18 May 2016)				
USGS ComCat	07:57:02.65	0.43	79.79	16.0
DD Relocation	07:57:02.09	0.38	80.03	40.7
IG-EPN	07:57:00.43	0.43	80.01	17.2
gCMT Centroid	07:57:08.10	0.43	80.04	27.5
Aftershock 2 (Mw 6.9, 18 May 2016)				
USGS ComCat	16:46:43.86	0.49	79.62	29.9
DD Relocation	16:46:41.38	0.39	79.88	43.3
IG-EPN	16:46:42.47	0.47	79.82	20.8
gCMT Centroid	16:46:49.20	0.30	80.02	33.6

Abbreviations: ComCat, Comprehensive Catalog; DD, double-difference; gCMT, Global Centroid Moment Tensor; USGS, U.S. Geological Survey.

The gCMT catalog (<http://www.globalcmt.org/>) provides moment tensor information, usually plotted as a beachball centered on the moment centroid. For large-magnitude earthquakes, however, the moment centroid may not correspond to the hypocenters reported by ISC and ComCat. Uncertainty in moment tensor catalogs has been explored by others (e.g., Frohlich & Davis, 1999; Kagan, 2003, and references therein), and we show only well-constrained CMT solutions following the criteria from Frohlich and Davis (1999; Figure 2, bottom row). The gCMT catalog of shallow thrust earthquakes provides supplemental information about the subducting slab geometry. Shallow dip thrust mechanisms with trench-parallel striking clusters in the Galera, Jama, and Manta segments are generally consistent in dip with the global Slab2.0 model (Hayes, 2018; Figure 2). In central Ecuador, a cluster of normal faulting events associated with intermediate-depth earthquakes (150–250 km) is also prominent in the data set (Figure 2e).

The Ecuador Seismic Network (IG-EPN) provides earthquake monitoring for the region (Alvarado et al., 2018; Font et al., 2013). The IG-EPN seismic catalog extends from the early 1990s to present (e.g., Beauval et al., 2013), and the 2016 mainshock-aftershock sequence was well recorded (see Table 1 for IG-EPN hypocenters of 2016 M_w 7.8, 6.7 and 6.9 events).

Local to regional earthquake location uncertainties from dense seismograph networks such as the IG-EPN can be an order of magnitude smaller than the uncertainties in the teleseismic catalogs (Wyss et al., 2011). However, the accuracy of arrival times, unmodeled velocity structure such as subducting slabs, and by limited azimuthal station coverage affects uncertainty in hypocenter determination at all scales. The IG-EPN catalog should provide more accurate epicenter determination in absolute space relative to teleseismic catalogs but may still exhibit spatial bias for offshore earthquakes due to the land-based station coverage. In this study, we use the IG-EPN catalog to assess the quality of the revised DD catalog.

2.2. Teleseismic Earthquake Relocation

Broadly, improvements to teleseismic catalog locations in South America incorporate the use of global 3-D velocity models to remove large-scale bias due to unmodeled velocity structure, waveform cross-correlation (CC) to improve arrival time accuracy, and/or use of differential time data to constrain relative hypocenters (e.g., Pesicek et al., 2014; Rietbrock & Waldhauser, 2004; Waldhauser & Schaff, 2007). The DD relocation and tomography method has been widely used in a variety of settings and scales to produce higher-resolution images of seismicity via improved clustering and relative location to illuminate fault zone structures and/or slip patterns that were not apparent in absolute catalog locations (e.g., Diehl et al., 2013; Pesicek et al., 2010; Waldhauser & Ellsworth, 2000; Waldhauser & Schaff, 2007; Zhang & Thurber, 2003). The further improvements in the relative locations can be achieved using precise differential arrival times via waveform CC (Waldhauser & Schaff, 2008). In the DD relocation procedure, minimizing the residuals between observed and calculated differential travel times yields improved relative locations between neighboring earthquakes (event pairs; Waldhauser & Ellsworth, 2000). The program teletomoDD is a modified version of DD tomography (Zhang & Thurber, 2003) that incorporates absolute time data and 3-D velocity structure with the differential time data adapted for global and regional teleseismic phases (Pesicek et al., 2010; Pesicek et al., 2014). TeletomoDD uses a 3-D velocity model and the pseudobending method (Um & Thurber, 1987) for ray tracing through a spherical Earth model with discontinuities (Koketsu & Sekine, 1998). The global P wave perturbation model MITP08 from Li et al. (2008) serves as the reference static 3-D Earth model. For Ecuador, a regional model derived from the MITP08 regridded to 0.7° spacing is nested with the 3-D global model and extends from -4.5°S to 4.5°N latitude, -84.7°W to -75.5°W longitude. We test location sensitivity to velocity by holding the regional model fixed and by conducting single iteration joint inversion for a new regional compressional wave model following the procedure described in Pesicek et al. (2014). Table S2 and Figure S1 in the supporting information provides the optimal damping parameters, and trade-off curves used to derive those parameters, for location only and joint inversion including velocity.

To build a catalog of differential times using teleseismic data, we use the phase onset times of first arrivals for individual earthquakes accessed through publicly available earthquake catalogs. The reviewed ISC Bulletin provides a unified and consistent teleseismic data set that includes the reexamination of phases, residuals, and focal depth solutions (Bondár & Storchak, 2011). Within the study area, the reviewed ISC Bulletin reports 1,512 events from 28 July 1961 to 31 December 2013. The ComCat data from 1 January 2014 to 19 November 2016 reports 229 events. The combined catalog includes a total of 1,741 events, including 141 reported aftershocks following the 2016 mainshock (Figure 2, top row). Catalog phase data include P, Pn, Pg, S, Sn, and Sg arrivals (primary phases) and pP (depth phase, ISC only). The inversion for the revised earthquake catalog uses catalog travel times from the ISC and ComCat and catalog-based differential time data (CTDT; Table S1). CTDTs are calculated for events with <100-km hypocentral separation for primary phases or 150-km separation for depth phases.

Differential time data are also calculated using CC of phases recorded on broadband stations archived with the IRIS DMC. For these so-called CCDTs, we apply CC on P, Pn, and pP phases reported in the teleseismic catalog using a filter passband of 0.75 to 2 Hz within the Geophysical Institute of Seismology Matlab Objects (GISMO) toolbox (Reyes & West, 2011). We retain CCDTs associated with CC coefficients above 0.80 for events with an event separation of 150 km. These thresholds are based on manual review of data. About 801 ISC and 219 ComCat events contained CC data. There is significantly less S data relative to P data for use in teleseismic DD location (Table S1). Also, only 15% of the total number of stations appear in both the ISC and ComCat catalogs and can be used to link the two catalogs via CCDTs. Of the CCDT data, only 25% directly links an ISC to ComCat event pair.

In summary, the absolute arrival times, CTDTs, and CCDTs for primary and depth phases are independent sets of datatypes used in the DD inversion process. These data types vary in quantity (Table S1) and quality. Therefore, we apply a hierarchical dynamic data weighting scheme to the inversion as similarly described in other DD studies (e.g., Pesicek et al., 2010; Waldhauser & Ellsworth, 2000). For all inversion iterations, the P wave times are always upweighted relative to the S wave data (Table S2). The initial iterations of the inversion update the locations and velocities primarily by absolute arrival time data. Subsequent iterations involve the CTDT data controlling the inversion. In the final iterations, the CCDT data provide the most control in determining the final hypocentral locations.

2.3. InSAR Observations and Modeling

A coseismic InSAR image represents the range distance difference measured in the satellite's line-of-sight (LOS) direction between two or more synthetic aperture radar (SAR) images acquired before and after the earthquake. This difference in LOS range is sensitive to the surface deformation on the order of the radar wavelength and is represented by the relative change in the interferometric phase on a pixel-by-pixel basis. As a result, InSAR has the capability to measure ground surface displacements with subcentimeter level precision. Descending track passes (heading angle: -168.04°) from the Sentinel 1-A sensor map the ground surface deformation due to the Pedernales mainshock and the large aftershocks. The Sentinel 1-A satellite is a C-band sensor operating at a wavelength of 5.6 cm with an ~ 20 (azimuth) \times 5 (range) m spatial resolution (De Zan & Guarnieri, 2006). The incidence angle of the acquisitions is $\sim 33.9^\circ$ at the center of the image swath.

The Sentinel-1A satellite has an orbital repeat time of 12 days and acquired SAR images after the mainshock and between the two large aftershocks on 18 May 2016. As a result, the 18 May Sentinel-1A acquisition provides a SAR image that allows us to separate the two aftershock ruptures. Previous studies used the Sentinel-1A and the ALOS-2 satellites data of the Pedernales mainshock and reported peak LOS displacements of 60–70 cm (He et al., 2017; Nocquet et al., 2017). Funning and Garcia (2019) analyzed the Sentinel 1-A InSAR pair for the M_w 7.8 mainshock and M_w 6.7 aftershock, but not the M_w 6.9 aftershock, and argued that the rainforest vegetation causes expected InSAR decorrelation in the region.

For consistency, we process deformation images for all three earthquakes using the same processing technique. SAR images acquired on 12 and 24 April 2016 produce the interferogram for the Pedernales mainshock (Figure 3a). For the 18 May events, the SAR image acquired on 18 May 2016 at 11:00:7.73 UTC paired with the 6 and 30 May 2016 SAR image produces the interferograms for the M_w 6.7 (7:57:2.65 UTC) and the M_w 6.9 (16:46:43.86 UTC) events, respectively (Figures 3b and 3c). The 12/24 April InSAR pair has a

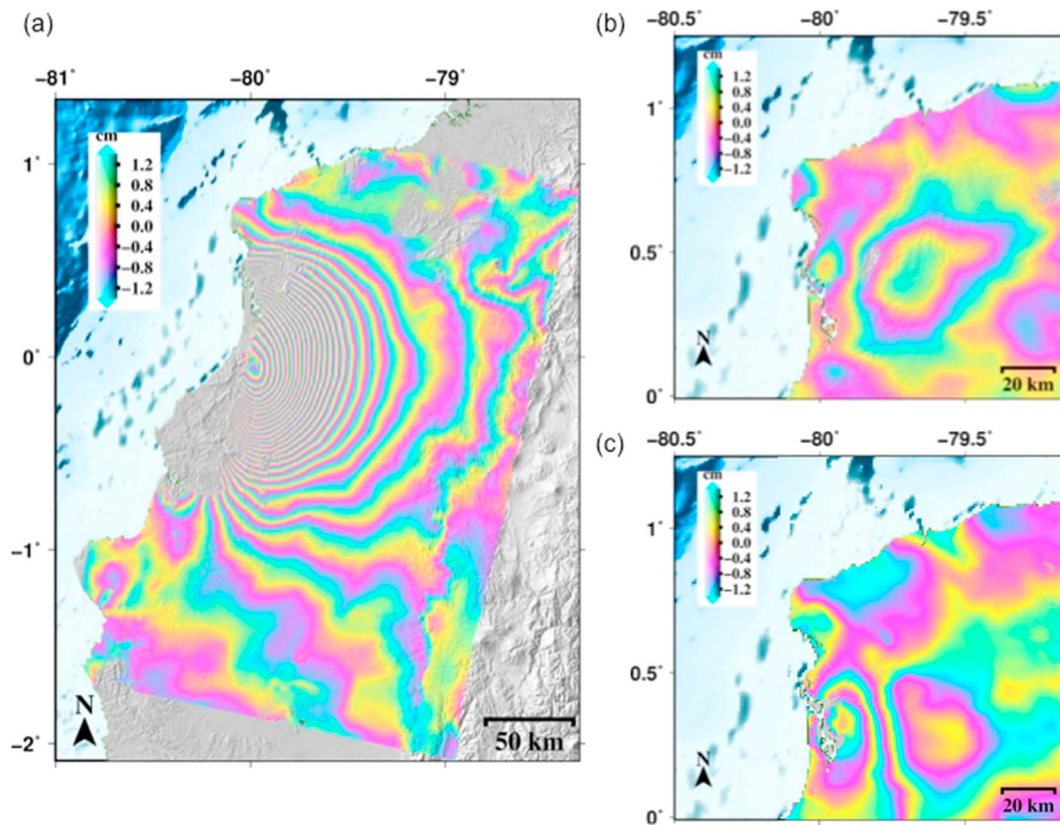


Figure 3. Wrapped Sentinel 1-A interferograms of the (a) 16 April 2016 mainshock (12/24 April interferometric synthetic aperture radar [InSAR] pair) and the (b) M_W 6.7 (6/18 May InSAR pair), and (c) M_W 6.9 (18/30 May InSAR pair) aftershocks of 18 May 2016.

perpendicular baseline of -17.59 m, whereas the 6/18 May and 18/30 May InSAR pairs have a perpendicular baseline of -76.17 and 59.61 m. Due to the small perpendicular baseline of less than 100 m, the spatial decorrelation might not be significant, but the dense vegetation in tropical climate attributed to the low coherence (<0.2) of Sentinel-1A interferograms requires a strong spatial filtering (Goldstein & Werner, 1998) to increase coherence. We remove topographic phases using the precise orbit ephemerides (<https://qc.sentinel1.eo.esa.int>) and the 1-arcsec (~ 30 m) global Shuttle Radar Topography Mission digital elevation model. The spectral diversity method provides precise coregistration of Sentinel-1A to avoid the discontinuous interferometric changes between bursts and subswaths (Yagüe-Martínez et al., 2016). We confirm that the primary interferometric phases in all interferograms do not contain significant atmospheric effects by checking existing weather forecast models (i.e., European Center for Medium-Range Weather Forecasts (ECMWF)'s European Reanalysis (ERA)-Interim and Generic Atmospheric Correction Online Service [GACOS]) and assessing the effects of the tropospheric delay on all the generated interferograms (Bekaert et al., 2015; Yu, Li, et al., 2017; Yu, Penna, et al., 2017). Residual phase ramps (due to baseline error or large-scale atmospheric artifact) in the original interferograms covering a large region are removed using a second order polynomial fitting assuming that the far-field deformation is negligible. We crop out a portion of the original interferogram over the epicenter area for further modeling.

We model the observed interferograms to verify the fault geometry and coseismic slip distribution. The most common approach for inverting earthquake interferograms is to numerically model a single rectangular dipping fault with uniform slip in an elastic half-space (Okada, 1985) by minimizing the misfit between the observations and model predictions from a least squares approach to find the optimal model parameters. Optimization approaches like these can lack the quantification of uncertainties associated with the model parameters. The model uncertainties are important to characterize when similar inversion results can yield different model parameters especially if the model is highly nonlinear. Therefore, we use a Bayesian

approach to solve the inverse problem because the formulations of posterior probability density functions (PDFs) provide statistical meaning on the model parameters. The Markov chain Monte Carlo (MCMC) algorithm with the Metropolis sampling approach is used to find the PDFs of physics-based source parameters (e.g., Anderson & Segall, 2013; Hastings, 1970; Mosegaard & Tarantola, 1995).

Interferograms containing a significantly large number of data points (in the millions) can limit the speed and efficiency of the modeling process. An effective way to reduce data points without losing resolution is to apply a two-dimensional quantization of the data set known as quadtree (e.g., Jónsson et al., 2002). The quadtree partitioning starts with the data set divided into four quadrants and the calculation of quadrant mean. If the root-mean-square (rms) scatter about the quadrant mean exceeds a variance threshold, the quadrant is subdivided into four subdivisions with associated means and subdivision continues until all quadrants meet a threshold criteria. For quadtree analysis of earthquake deformation, the densest squares should sample the region nearest to and incorporating the surface projection of the fault (Figure S4).

We use the Geodetic Bayesian Inversion Software (GBIS) to model the 2016 mainshock and the 18th May aftershock interferograms (e.g., Bagnardi & Hooper, 2018). This recently developed software follows a Bayesian approach using the MCMC algorithm and quadtree data sampling to invert for surface deformation from a variety of analytical models. For application to earthquake sources, we apply the Okada model for a dipping fault with uniform slip. Further information about GBIS, quadtree, and PDF results appears in the supporting information (Figure S4–S7).

3. Results

3.1. Teleseismic DD Locations

The merging of two teleseismic catalogs, inclusion of an updated 3-D velocity model and use of differential time data to constrain relative location, results in significant hypocentral changes in the Ecuador teleseismic catalog (Figures 2 and 4). We compared relocation through the global DD model (DD-only) with relocation solutions using joint inversion (DD-tomo). For the Ecuador-Columbia shallow subduction zone, the MITP08 model does not image a dipping high-velocity anomaly indicative of a subducting slab. Our tomographic inversion (Figure 4), plotted relative to ak135, does image dipping velocity anomalies that trend parallel to the Slab2.0 earthquake-derived slab. Tomographic inversion results in significant residual reduction from 0.55 rms residual time for DD-only to 0.28 rms for DD-tomo, but changes in hypocentral parameters appear minor (Table S3). Within the seismogenic zone, here defined as extending from trench to ~100 km, hypocentral changes were ~8 km in epicenter and ~3 km in depth, which are on par with the absolute uncertainties reported for the Sunda subduction zone (10, 11-km latitude, longitude and 7-km depth; Pesicek et al., 2010). Both Ecuador DD catalogs showed similar spatial patterns in seismicity, and we present the DD-tomo catalog as the preferred catalog (Data Set S1 in the supporting information) for discussion.

There are significant hypocentral changes between the DD-tomo catalog and the original ISC and ComCat teleseismic catalogs. First, the median epicentral difference records a shift of the seismicity ~26 km to the southwest (Figure 4a and Table S3). The large number and clustering of intermediate-depth earthquakes biases catalog comparisons, so we separate the changes to those reflecting the full catalog and changes reflecting the shallow subduction zone (0- to 100-km depth). Within the shallow subduction zone, the systematic shift is ~25 km to the southwest (Table S3). The DD locations appear more tightly clustered, as expected for a relative location procedure, especially in the Galera and Jama seismic regions (Figure 2). It is also apparent that many aftershocks occur in the same seismicity clouds defined by earthquakes occurring prior to 2016 (Figure 2), a finding noted in previous studies of the 2016 Pedernales sequence (e.g., Nocquet et al., 2017; Vaca et al., 2018).

The depth resolution of the ISC and ComCat is poor, as reflected in the large set of fixed 10-km depth solutions for shallow events (Figures 4 and 5). The DD hypocenters are deeper than the ISC and ComCat catalogs by a median ~21 km (median absolute deviation 10 km), and in the shallow subduction zone of ~15 km (median absolute deviation 10.5 km). The DD locations form an east dipping feature, however, that is consistent with the Slab2.0 model at shallow depths (<100 km), and down to 250 km depth, the DD catalog defines a more smoothly dipping slab than Slab2.0 (Figure 4). The derived regional velocity model

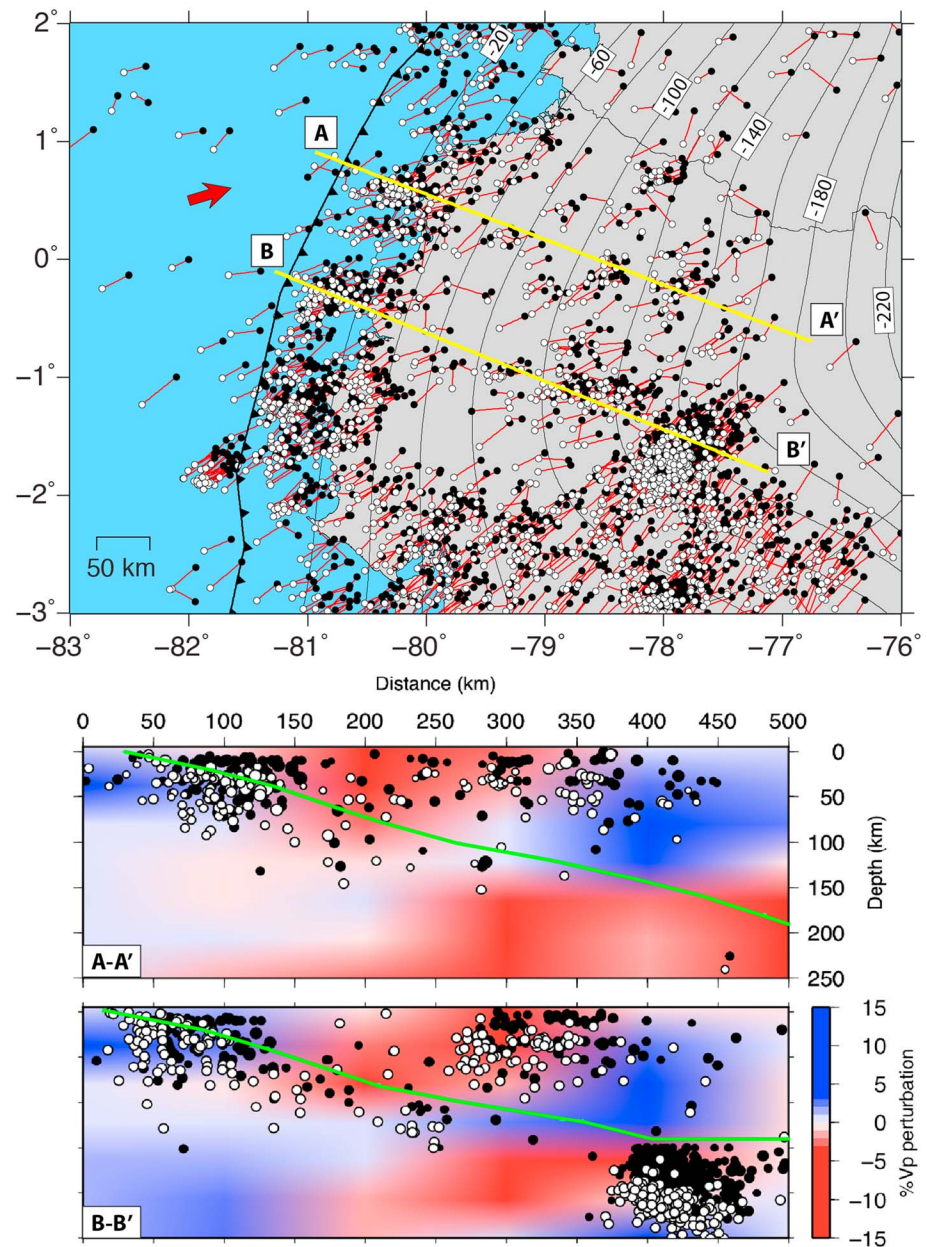


Figure 4. Comparison of the teleseismic International Seismological Centre/Comprehensive Catalog (black circles) and the double-difference catalog (white circles). The top epicentral map highlight the ~25-km southwest shift in epicenters relative to the oblique convergence (arrow) of the Carnegie Ridge. The red bars link initial and relocation to highlight systematic trends. Cross-section locations are taken perpendicular to Slab2.0 depth contours (20-km interval, negative numbers indicate depth to top of the slab) that crosses two distinct seismic clusters on the megathrust (A-A' and B-B') showing; Cross sections of earthquake catalogs (circles), Slab2.0 top of the slab (green), and regional velocity perturbation relative to ak135 model.

contains slow velocities below 100 km (Figure 4) that are left for future study. Interpretation and exploration of location uncertainty focus on the shallow subduction zone earthquakes.

TeletomoDD uses a least squares with QR factorization inversion technique that precludes the calculation of formal location uncertainties. We use a bootstrap approach to estimate uncertainty by running 50 inversions that each have 10% of each type of phase and differential time dataset randomly removed. The difference in epicenter location (km), focal depth (km), and origin time (s) reflects uncertainty in location due to phase information but does not reflect absolute location uncertainty due to velocity model. Location changes

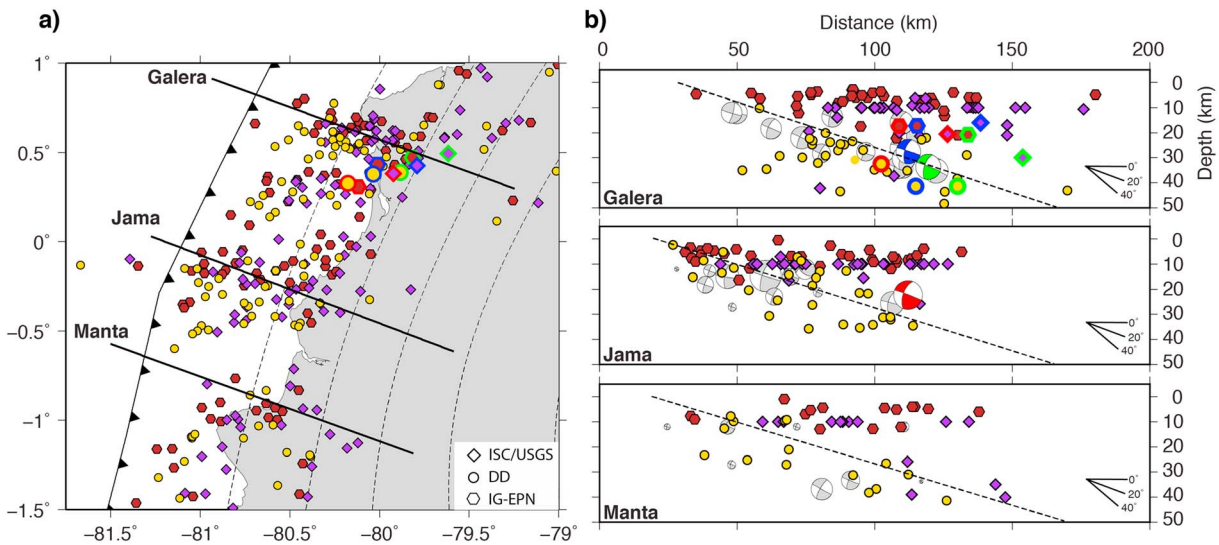


Figure 5. (a) Epicentral comparison of in common International Seismological Centre (ISC)/Comprehensive Catalog (purple diamonds), double-difference (DD; yellow circles), and IG-EPN (brown hexagon) catalog events. The 2016 M_W 7.8 mainshock and M_W 6.7 and M_W 6.9 aftershocks are outlined in red, blue, and green respectively. (b) Cross sections for the Galera, Jama, and Manta seismic regions are shown comparing the three catalog locations with respect to the Slab2.0 model (dashed line). Global Centroid Moment Tensor solutions are shown at centroid location.

due to use of different regional 3-D velocity models were discussed previously. We take the standard deviation of the location differences for each event (full data relocated event differenced from 50 relocations with 10% data randomly removed) and compute the mean of those events to derive an estimate of relative location uncertainty for the entire DD catalog (Table S3). The mean change in epicenter is ~ 2 km, in depth is 1.8 km, and in origin time is 0.37 s. Within the seismogenic zone (above 100-km depth), the mean change is 1.30 km in epicenter, 1.33 km in depth, and 0.24 s in origin time. These values best estimate the relative location uncertainty in the data set in areas of highly clustered seismicity and do not reflect absolute location uncertainty for events not well-linked through differential time data.

Network locations from the IG-EPN (<http://www.igepn.edu.ec/solicitud-de-datos>, last accessed 4 September 2017) provide events from 2012 through 2016 for comparison with the teleseismic catalogs. We discard fixed event depth solutions (10 km) from the IG-EPN catalog and match IG-EPN events to the ISC/ComCat (214 events) and DD catalog (208 events) by associating in space and requiring origin time within 60 s. Both the ISC/ComCat and DD catalogs have a median epicentral difference of ~ 20 km relative to the IG-EPN catalog (Table S3). Depth differences between the catalogs are larger (Table S3). Within the seismogenic zone, Figure 5b illustrates that the DD locations are able to define the location of the slab and show that the seismicity delineates a dipping feature parallel to the Slab2.0 model ($\sim 20^\circ$ to the east) and consistent with the dip of gCMT solutions across the Galera, Jama, and Manta clusters (Figure 5) and removes the subhorizontal trends notable in the IG-EPN and ISC/ComCat catalogs. Relocated shallow seismic clusters locate near the bottom and top of the Slab2.0 subduction interface and dip $20\text{--}25^\circ$ east, consistent with the plate interface proposed in Font et al. (2013).

3.2. InSAR Models

The three modeled interferograms generally fit the InSAR data well, and the small residual deformation (Figure 6) mostly reflects tropospheric delay rather than earthquake signal. Inherent to the Ecuador data, both the mainshock and aftershock 1 can only resolve a one-sided InSAR lobe, whereas aftershock 2 can be resolved with a complete lobe. Although the interferograms are only limited to onshore observations, we invert for uniform slip on a fault and calculated moment for the three events based on the InSAR models (Table 2).

InSAR-derived slip information is summarized in Table 2. The optimal solution for the mainshock defines a $79\text{-km} \times 45\text{-km}$ slip area (Figures 6a–6c). Relative to the gCMT and USGS slip model, the InSAR mainshock strike is $16\text{--}17^\circ$ more northward and 15 to 20° steeper (Figure 6b). Although there are discrepancies in the

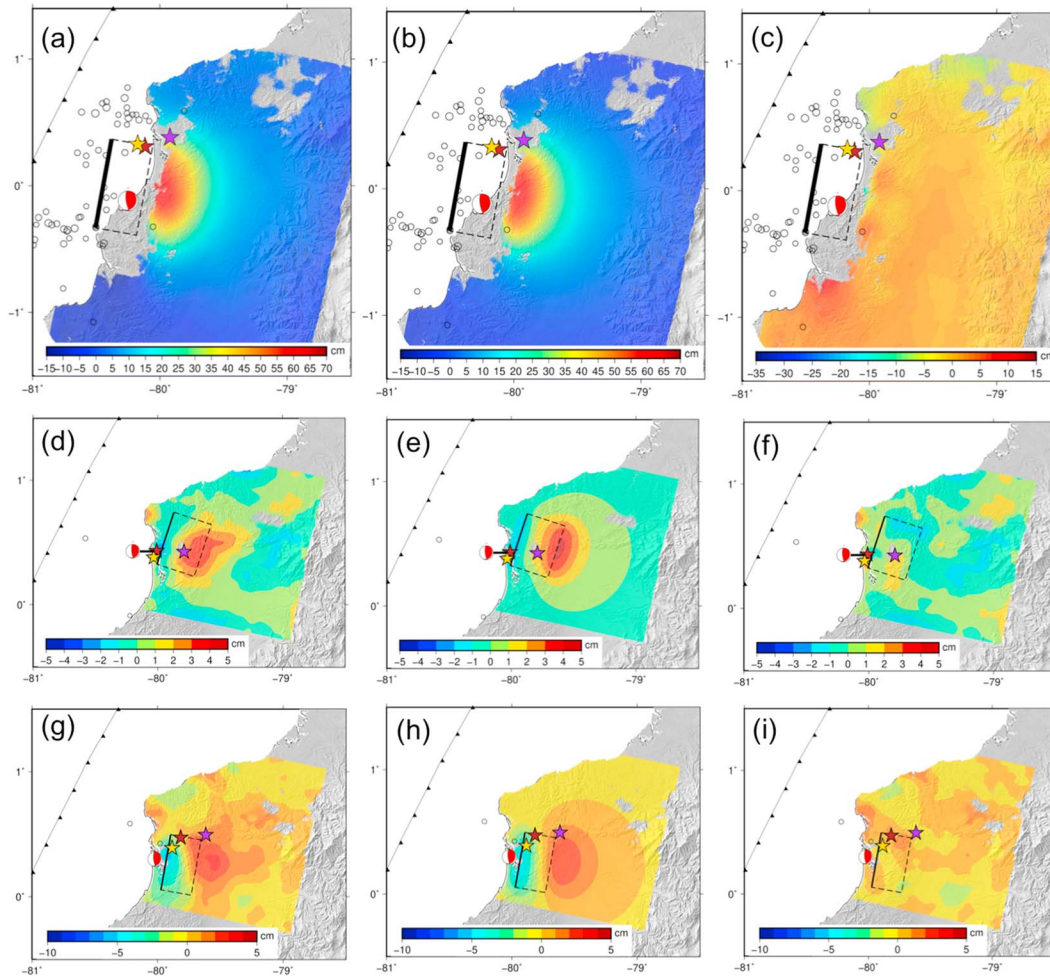


Figure 6. Unwrapped interferometric synthetic aperture radar line-of-sight observations (left column), unwrapped synthetic model interferogram (middle column), and model residual interferogram (right column) for the (a–c) mainshock, (d–f) aftershock 1, and (g–i) aftershock 2. For each event, the Comprehensive Catalog (purple star), double-difference (yellow star), and IG-EPN epicenters (brown star) are shown with the gCMT centroid (red beachball). The digital elevation model is plotted under the interferogram. All earthquakes (open circles) occurring between the synthetic aperture radar acquisition times for each interferogram are also shown. The dashed boxes represent the surface projected fault area of the best fitting dislocation plane from co-seismic interferometric synthetic aperture radar modeling and the thickened edges represent the shallow end of the fault plane.

fault geometry between the InSAR and seismic solutions, the NNE strike direction and thrust fault dip range ($<45^\circ$) are similar. The InSAR-derived fault depth (26.5 km) reflects the depth to the bottom of the modeled fault, which is 4–6 km deeper than the center of slip. For aftershock 1, the uniform slip area is resolved inland on a shallow, 49-km \times 39-km plane (Figures 6d–6f), and when compared to the gCMT solution, the strike is

Table 2
Summary of InSAR and Seismic Source Models

Model	Longitude ($^\circ$)	Latitude ($^\circ$)	Strike ($^\circ$)	Dip ($^\circ$)	Length (km)	Width (km)	Depth (km)	Slip (m)	Moment ($\times 10^{20}$ N*m)	M_W
Mainshock - USGS	-79.926	0.352	26	16	-	-	20.6	-	7.05	7.8
Mainshock - gCMT	-80.250	-0.120	27	21	-	-	22.3	-	5.93	7.8
Mainshock - InSAR	-80.121	-0.040	10.3	36.3	79	45	26.5	5.050	5.74	7.81
Aftershock 1 - gCMT	-80.040	0.430	28	18	-	-	27.5	-	0.141	6.7
Aftershock 1 - InSAR	-79.640	0.437	18	7	49	38	14.8	0.143	0.085	6.59
Aftershock 2 - gCMT	-80.020	0.300	28	21	-	-	33.6	-	0.253	6.9
Aftershock 2 - InSAR	-79.690	0.233	10	19.2	50	33	25.0	0.215	0.114	6.67

Abbreviations: gCMT, Global Centroid Moment Tensor; InSAR, interferometric synthetic aperture radar; USGS, U.S. Geological Survey.

10° northward and 11° shallower. The seismic moment derived from InSAR corresponds to a M_W 6.59 coseismic event and is underestimated compared to the gCMT-derived M_W 6.7. Of the three InSAR models, the optimal fault area for aftershock 2 (Figures 6g-6i) is located farthest from the coast and has the smallest slip area (50 km × 33 km). The InSAR-derived seismic moment corresponds to an M_W 6.6 event, again underestimated when compared to the gCMT of M_W 6.9, but still larger than the first aftershock. The optimal fault strike is 10° NNE with ~19° dip to the east. The InSAR fault strike for aftershock 2 is similar to the mainshock and oriented 18° northward from the gCMT strike; the dip is close to the gCMT dip (21°).

Slip area was the most problematic parameter to constrain for the inversion of aftershock 2, and a minimum fault length of 50 km was set in order to derive a considerable moment larger than aftershock 1. Both aftershocks have underestimated InSAR-derived moments that could be explained from studies of several earthquakes that have shown a slight tendency for InSAR-derived moments to be smaller than those reported in the gCMT catalog, attributed to low signal-to-noise ratios, substantial offshore deformation, and small surface deformation due to earthquake depth (Weston et al., 2011).

The relocated teleseismic (DD) and local (IG-EPN) epicentral locations of the mainshock, aftershock 1, and aftershock 2 agree well with each other and fall within the InSAR-derived slip areas (Figure 6). The ComCat epicenters lie outside the fault area for the mainshock and aftershock 2 and within the slip area of aftershock 1. The InSAR depths for the three events are more consistent with the ComCat hypocenter and gCMT centroid depths, but the DD solutions place these events about 10 to 15 km deeper (compare Tables 1 and 2).

4. Discussion

4.1. Teleseismic Locations Along the Ecuador-Columbia Subduction Zone

One goal of this study is to improve teleseismic event catalogs in order to better define the geometry and extent of the seismogenic zone where local data are not available. The uncertainty calculations via bootstrap for the Ecuador DD catalog assume that the 3-D velocity model correctly reflects large-scale heterogeneity, such as subducting lithosphere. The global MITP08 (Li et al., 2008) model contains a high velocity, subducting slab under Peru and Chile but not in the Ecuador region. Instead, the V_p perturbation calculated relative to ak135 indicates slow velocities where a fast subducting slab is expected and likely reflects a lack of earthquake data prior to 2008. The revised single iteration regional velocity model calculated in this study, shown in Figure 4 plotted relative to ak135, does contain faster velocities within the shallow seismogenic zone and provides a more realistic 3-D velocity model under Ecuador, but large areas of slow velocity present in the starting MITP08 model remain. Future work to further improve the tomographic images for the Ecuador subduction zone is required to yield more accurate absolute depths. However, the general agreement with DD catalog dip with the expected slab structure of the subducting Nazca plate supports the bootstrap-derived low relative uncertainty values.

The ~25-km systematic shift to the southwest in the DD catalog (Figure 4) is possibly due to azimuthally biased station coverage to the north and east. Globally, observations from stations located east, on South America, and to the north, in North America, provide dense observations for earthquakes in Ecuador. Earthquake catalogs can be biased toward dense station coverage, such as offshore earthquakes being pulled landward due to stations located on land, and such spatial bias in global earthquake catalogs has been documented in other subduction zones (e.g., Syracuse & Abers, 2009). The epicentral agreement between the DD epicenters for the three largest earthquakes, InSAR solutions, and relocation using local seismic stations (Nocquet et al., 2017) supports the epicentral shift noted in the DD catalog. It is also of note that the systematic shift occurs when either the global MITP08 model or the tomography derived regional velocity model is used, suggesting that any model that contains some slab structure yields this change.

4.2. Interseismic Earthquakes

Recent studies provide new interpretations on the rupture histories of the 1906 to 2016 great megathrusts. The 1942, 1958, and 1979 rupture areas are inferred to be neighboring each other and cumulatively overlap with the 1906 rupture extent, a characteristic termed “the Ecuador supercycle” by Nocquet et al. (2017). However, Yoshimoto et al. (2017) estimated the slip distribution of the 1906 event (corresponding to a M_W 8.4) to be exclusively located updip near the trench, in an area that behaves aseismically following the 2016 mainshock (Rolandone et al., 2018). The Yoshimoto study concluded that the 1906 rupture did

not overlap with the deeper 1942, 1958, 1979, and 2016 rupture areas and/or asperities. Yi et al. (2018) suggested that the 1942 and 2016 Ecuador events, similar in size and location, did not overlap, whereas other studies (He et al., 2017; Nocquet et al., 2017; Ye et al., 2016; Yoshimoto et al., 2017) suggest they did overlap.

Prior to the 2016 M_w 7.8 Pedernales earthquake, interseismic seismicity indicates persistent seismic clusters along the megathrust (Figure 2). These well-defined clusters define in the Galera, Jama, and Manta seismic regions were observed in global catalogs prior to the Pedernales event (Font et al., 2013). Teleseismic events recorded since ~1960 show that these clusters located offshore central to northern Ecuador are characterized by alignments of north-northwest (perpendicular to trench) trending earthquakes separated by notable seismic gaps or only small event clusters. The DD catalog confirms that the seismic clusters terminate near the coast, particularly for the Galera and Jama region, and that onshore earthquakes (downdip) occurring during the interseismic cycle appear more spatially diffuse. The Pedernales mainshock slip occurs within an area bounded by the Galera and Jama clusters that did not host significant seismicity during the interseismic cycle.

4.3. Large Megathrust Earthquakes and the 2016 Pedernales Sequence

Observations of overlapping seismic asperities can reflect persistent frictional or mechanical fault properties of the megathrust that are reused over multiple seismic cycles. Asperities, or regions of strong coupling, were imaged using geodetic data just prior to the 2016 earthquake via interseismic locking (coupling) models reported in Chlieh et al. (2014) and Nocquet et al. (2017; updated model from Nocquet et al., 2014). The plate locking models agree well and image similar asperities relative to the locations of historic earthquakes. Nocquet et al. (2017) suggest that propagation of rupture during large earthquakes does not reach updip to the trench. For discussion, we focus on the rough model (minimum coupling) presented in Chlieh et al. (2014), rather than the smooth model (maximum coupling), as the former offers evidence of up to seven discrete asperities, whereas the latter model tends to average neighboring asperities. We plot the rough coupling model (also referred here as the Chlieh model) and identified four highly coupled asperity regions (A1-A4) where plate coupling is >0.4 (Figure 7b). We also show the coupling model from Nocquet et al. (2017) as contour intervals for comparison.

Both the 1942 epicenter (Mendoza & Dewey, 1984) and the 2016 mainshock are located offshore within asperity A3. The coseismic InSAR deformation indicates that the mainshock ruptured on asperity A3 (Figure 7). When the rapidly calculated USGS mainshock (finite-fault) slip model (earthquakes.usgs.gov, 2016) is adjusted in accordance with the relative offset between the DD location and the USGS/ANSS ComCat mainshock location, mainshock slip moves offshore and the down-dip edge of slip agrees better with the InSAR deformation data (Figure 7a). The offshore slip extent matches spatially to the fault area from InSAR modeling and aligns better with the local data derived mainshock slip distribution and epicenter from Nocquet et al. (2017). This confirms that the DD epicenter is more accurate in space than the original USGS/ANSS ComCat location.

The 18 May aftershock epicenters are located northeast from the mainshock in the DD catalog (Figure 7). The InSAR models indicate that the two largest aftershocks both ruptured northeast from the northern-east edge of the mainshock rupture in a narrow seismic gap between the 1958 and 1942/2016 rupture regions. In the Chlieh model, a distinct highly locked asperity region (A2) is located on the peninsula within the Galera region. There is small overlap between the asperity region A2 and the two 18 May aftershock InSAR fault region. Chlieh et al. (2014) noted this asperity and considered a future large earthquake in that area, but it is now regarded as the aseismic Punta Galera-Mompiche Zone (PGMZ; Vaca et al., 2018). The Nocquet and Chlieh models indicate that the asperity region A2 is moderately to highly coupled, while the two largest Pedernales aftershocks occur in an unstable seismic slip region abutting the PGMZ.

In the teleseismic catalog, the Pedernales aftershocks occur mostly within the Galera and Jama seismic clusters that bound the entire segment of the mainshock rupture instead of occurring within or surrounding the slip asperities. Seismicity after the 18th May aftershocks continue to occur within those interplate segments as well but also to the northeast from the Galera cluster, separate from the mainshock area. The DD locations highlight the spatial relationships between the great $M_w > 7.5$ epicenter locations and aftershock seismicity in relation to interplate coupling. The Pedernales aftershocks show that strong (magnitude 6.0-6.9) seismic events present considerable hazard for coastal to inland regions in northern

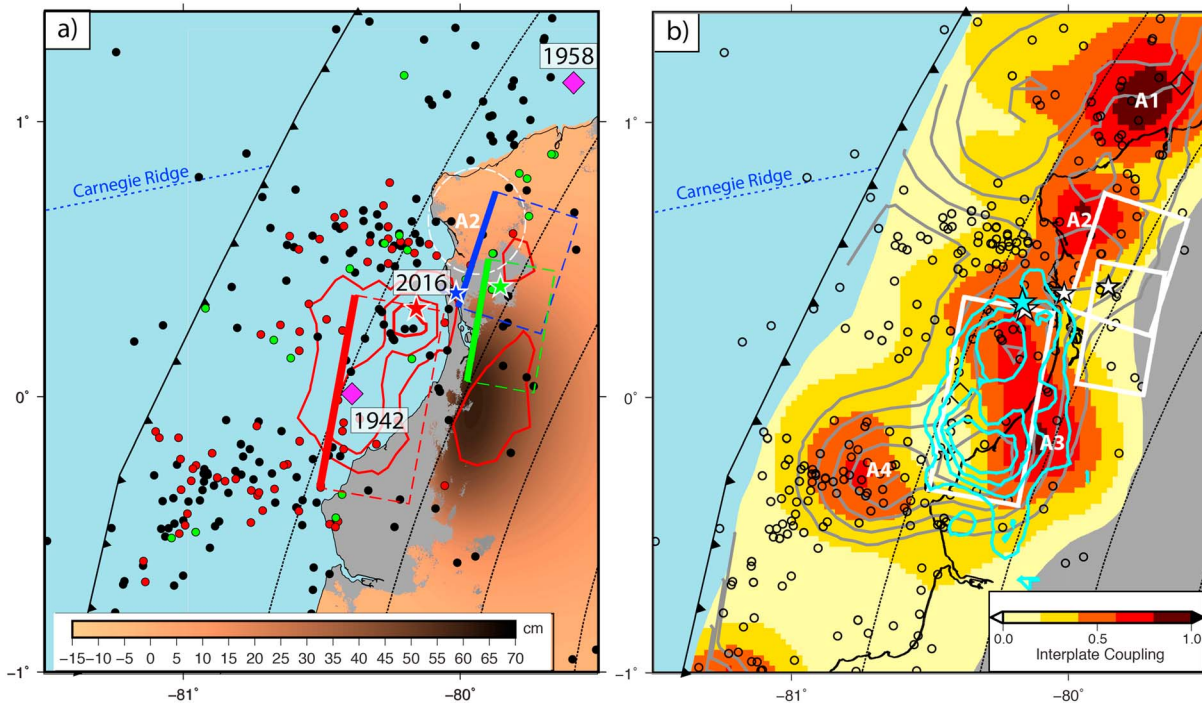


Figure 7. (a) Double-difference (DD) teleseismic catalog locations and coseismic interferometric synthetic aperture radar (InSAR) observations for the northern Ecuador margin. Seismicity before the 2016 mainshock (black circles). The 2016 seismicity sequence locations are indicated by the following: 16 April mainshock and aftershocks before 18 May events (red), 18 May events for aftershock 1 and following (blue), and aftershock 2 and following (green). The 1942 and 1958 epicenters (Mendoza & Dewey, 1984) are shown (magenta diamonds). The 2016 mainshock coseismic interferogram is shown in the copper to black gradient. The InSAR fault area of the mainshock, aftershock 1 and 2 are outlined in red, blue, and green respectively and the stars show their DD epicentral locations. The mainshock slip model (red 1 m contour lines) from the USGS is plotted relative to the relocated DD epicenter (red star), as discussed in the main text. (b) The interseismic coupling from Chlieh et al. (2014) is illustrated in the yellow to dark red scale indicating low to high coupling (1 is 100% coupling). Four distinct regions of high interplate coupling are noted (A1-A4). The black contour lines (20% coupling interval) and cyan contour lines (1-m slip interval) indicate the coupling model and mainshock slip model values, respectively, from Nocquet et al. (2017), respectively. The relocated DD mainshock location agrees with the epicenter from Nocquet et al. (2017; cyan star). The InSAR fault areas and associated DD event locations are shown in white. The DD seismicity is shown as unfilled circles.

Ecuador. Currently, asperity regions A1 and A3 have hosted the locations of large megathrust earthquakes but A2 has not. High-resolution earthquake locations and InSAR data suggest that rupture along Ecuador associated with large to great earthquakes does not overlap with the location of moderate to smaller earthquakes nor with areas of aseismic slip.

5. Conclusion

Unique to this study, we show that Sentinel 1-A InSAR data can identify measurable surface deformation for the two large $M_{w} 6.5+$ aftershocks when satellite passes are sufficiently close in time. However, precise quantification of slip and moment for these events is limited by noise due to unmodeled atmospheric and/or vegetation conditions. The InSAR data are here used to confirm teleseismic DD relocations and explore depth uncertainty. The InSAR results, however, show that large aftershocks were focused to the northeast of the mainshock along areas of the megathrust fault that exhibit moderate to high coupling but failed to slip during the 2016 $M_{w} 7.8$ Pedernales earthquake. Our result confirms previous studies showing that InSAR can contribute to assessing the quality of global seismic earthquake catalogs (e.g., Weston et al., 2012).

We present a high-resolution teleseismic catalog of relative DD hypocenter locations (1961-2016) along the Ecuador subduction margin that exhibit epicentral shifts ~ 25 km southwest. The shift, while large, yields teleseismically derived locations that are consistent with local seismic network solutions and better match InSAR-derived deformation data. The DD catalog shows tighter alignment of persistent event clusters along the megathrust over the seismic cycle and reproduces many of the segmentation features of the Ecuador subduction zone reported for the Pedernales sequence using local seismic data (Font et al., 2013; Rolandone et al., 2018). The DD relocations confirm that the 2016 mainshock epicenter occurred offshore, similar to

Nocquet et al. (2017), rather than the near-on-shore location provided in the ComCat. The DD catalog relative locations, which link the ComCat rapid locations to the reviewed ISC historic catalog, better reproduce the slab dip required by gCMT data and the InSAR data presented here, suggesting that the relative relocations are improved relative to the standard rapid global catalog. This study affirms that using differential times that link new seismicity to established catalogs can yield important improvements to absolute locations in rapidly produced earthquake catalogs. Improvements to the Ecuador DD catalog, especially in depth, can be calculated in the future through improved 3-D regional velocity models constrained by local seismic catalogs (i.e., Beauval et al., 2013; Font et al., 2013; Pontoise & Monfret, 2004) and by incorporating the seismic data obtained by the international rapid response team (e.g., Font et al., 2016).

Acknowledgments

We thank Mohamed Chlieh and Jean-Mathieu Nocquet for providing interseismic coupling models and Jean-Mathieu once again for their mainshock slip model. Comments by the Editor and two anonymous reviewers resulted in substantial improvements to the manuscript. Earthquake teleseismic waveforms for cross correlation were obtained from the IRS DMC. Sentinel-1A data were obtained from Sentinels scientific data hub in Copernicus initiative. Internal financial support from the SMU Huffington Department of Earth Sciences, Institute for the Study of Earth and Man at SMU, and Dissertation Fellowship at SMU. Figures were made using Generic Mapping Tool (Wessel & Smith, 1998). Additional data can be found in the supporting information. Seismic phase data and interferograms are archived at the SMU Radar Lab in the “2016 Ecuador Earthquakes” link at <https://smu.edu/radarlab>.

References

- Alvarado, A., Ruiz, M., Mothes, P., Yepes, H., Segovia, M., Vaca, M., et al. (2018). Seismic, volcanic, and geodetic networks in Ecuador: Building capacity for monitoring and research. *Seismological Research Letters*, 89, 432–439. <https://doi.org/10.1785/0220170229>
- Anderson, K., & Segall, P. (2013). Bayesian inversion of data from effusive volcanic eruptions using physics-based models: Application to Mount St. Helens 2004–2008. *Journal of Geophysical Research: Solid Earth*, 118, 2017–2037. <https://doi.org/10.1002/jgrb.50169>
- Bagnardi, M., & Hooper, A. (2018). Inversion of surface deformation data for rapid estimates of source parameters and uncertainties: a Bayesian approach. *Geochemistry, Geophysics, Geosystems*, 19(7), 2194–2211. <https://doi.org/10.1029/2018GC007585>
- Beauval, C., Yepes, H., Palacios, P., Segovia, M., Alvarado, A., Font, Y., et al. (2013). An earthquake catalog for seismic hazard assessment in Ecuador. *Bulletin of the Seismological Society of America*, 103(2A), 773–786. <https://doi.org/10.1785/0120120270>
- Bekaert, D. P. S., Walters, R. J., Wright, T. J., Hooper, A. J., & Parker, D. J. (2015). Statistical comparison of InSAR tropospheric correction techniques. *Remote Sensing of Environment*, 170, 40–47. <https://doi.org/10.1016/j.rse.2015.08.035>
- Bilek, S. L. (2010). Seismicity along the South American subduction zone: Review of large earthquakes, tsunamis, and subduction zone complexity. *Tectonophysics*, 495(1–2), 2–14. <https://doi.org/10.1016/j.tecto.2009.02.037>
- Bondár, I., & Storchak, D. (2011). Improved location procedures at the International Seismological Centre. *Geophysical Journal International*, 186(3), 1220–1244. <https://doi.org/10.1111/j.1365-246X.2011.05107.x>
- Chen, P. F., Bina, C. R., & Okal, E. A. (2001). Variations in slab dip along the subducting Nazca Plate, as related to stress patterns and moment release of intermediate-depth seismicity and to surface volcanism. *Geochemistry, Geophysics, Geosystems*, 2(12), GC000153. <https://doi.org/10.1029/2001GC000153>
- Chlieh, M., Mothes, P. A., Nocquet, J. M., Jarrin, P., Charvis, P., Cisneros, D., et al. (2014). Distribution of discrete seismic asperities and aseismic slip along the Ecuadorian megathrust. *Earth and Planetary Science Letters*, 400, 292–301. <https://doi.org/10.1016/j.epsl.2014.05.027>
- Collot, J. Y., Sanclemente, E., Nocquet, J. M., Leprêtre, A., Ribodetti, A., Jarrin, P., et al. (2017). Subducted oceanic relief locks the shallow megathrust in central Ecuador. *Journal of Geophysical Research: Solid Earth*, 122, 3286–3305. <https://doi.org/10.1002/2016JB013849>
- De Zan, F., & Guarnieri, A. M. (2006). TOPSAR: Terrain observation by progressive scans. *IEEE Transactions on Geoscience and Remote Sensing*, 44(9), 2352–2360. <https://doi.org/10.1109/TGRS.2006.873853>
- Diehl, T., Waldhauser, F., Cochran, J. R., Kamesh Raju, K. A., Seeber, L., Schaff, D., & Engdahl, E. R. (2013). Back-arc extension in the Andaman Sea: Tectonic and magmatic processes imaged by high-precision teleseismic double-difference earthquake relocation. *Journal of Geophysical Research: Solid Earth*, 118, 2206–2224. <https://doi.org/10.1002/jgrb.50192>
- El Hariri, M., Bilek, S. L., Engdahl, E. R., DeShon, H. R., & Bisrat, S. T. (2013). Along-strike variability of rupture duration in subduction-zone earthquakes. *Journal of Geophysical Research: Solid Earth*, 118, 646–664. <https://doi.org/10.1029/2012JB009548>
- Engdahl, E. R., van der Hilst, R., & Buland, R. (1998). Global teleseismic earthquake relocation with improved travel times and procedures for depth determination. *Bulletin of the Seismological Society of America*, 88(3), 722–743.
- Font, Y., Ruiz, M. C., Alvarado, A. P., Mercerat, D., Beck, S. L., Leon Rios, S., et al., (2016). International postseismic response after the Mw=7.8 April 16, 2016 Pedernales Earthquake in Ecuador, American Geophysical Union, Fall Meeting 2016, abstract #T51E-2977.
- Font, Y., Segovia, M., Vaca, S., & Theunissen, T. (2013). Seismicity patterns along the Ecuadorian subduction zone: New constraints from earthquake location in a 3-D a priori velocity model. *Geophysical Journal International*, 193(1), 263–286. <https://doi.org/10.1093/gji/ggs083>
- Frohlich, C., & Davis, S. D. (1999). How well constrained are well-constrained T, B, and P axes in moment tensor catalogs? *Journal of Geophysical Research*, 104(B3), 4901–4910. <https://doi.org/10.1029/1998JB900071>
- Funning, G. J., & Garcia, A. (2019). A systematic study of earthquake detectability using Sentinel-1 Interferometric Wide-Swath data. *Geophysical Journal International*, 216(1, 1 January 2019), 332–349. <https://doi.org/10.1093/gji/ggy426>
- Goldstein, R. M., & Werner, C. L. (1998). Radar interferogram filtering for geophysical applications. *Geophysical Research Letters*, 25(21), 4035–4038. <https://doi.org/10.1029/1998GL900033>
- Gutscher, M. A., Malavieille, J., Lallemand, S., & Collot, J. Y. (1999). Tectonic segmentation of the North Andean margin: Impact of the Carnegie Ridge collision. *Earth and Planetary Science Letters*, 168(3–4), 255–270. [https://doi.org/10.1016/S0012-821X\(99\)00060-6](https://doi.org/10.1016/S0012-821X(99)00060-6)
- Hastings, W. K. (1970). Monte Carlo sampling methods using Markov chains and their applications. *Biometrika*, 57(1), 97–109. <https://doi.org/10.1093/biomet/57.1.97>
- Hayes, G. (2018). Slab2—A comprehensive subduction zone geometry model: U.S. Geological Survey data release. <https://doi.org/10.5066/F7PV6JNV>
- He, P., Hetland, E. A., Wang, Q., Ding, K., Wen, Y., & Zou, R. (2017). Coseismic slip in the 2016 Mw 7.8 Ecuador earthquake imaged from Sentinel-1A radar interferometry. *Seismological Research Letters*, 88(2A), 277–286. <https://doi.org/10.1785/0220160151>
- Jónsson, S., Zebker, H., Segall, P., & Amelung, F. (2002). Fault slip distribution of the 1999 Mw 7.1 Hector Mine, California, earthquake, estimated from satellite radar and GPS measurements. *Bulletin of the Seismological Society of America*, 92(4), 1377–1389. <https://doi.org/10.1785/0120000922>
- Kagan, Y. Y. (2003). Accuracy of modern global earthquake catalogs. *Physics of the Earth and Planetary Interiors*, 135(2–3), 173–209. [https://doi.org/10.1016/S0031-9201\(02\)00214-5](https://doi.org/10.1016/S0031-9201(02)00214-5)

- Kanamori, H., & McNally, K. C. (1982). Variable rupture mode of the subduction zone along the Ecuador-Colombia coast. *Bulletin of the Seismological Society of America*, 72(4), 1241–1253.
- Kelleher, J. A. (1972). Rupture zones of large South American earthquakes and some predictions. *Journal of Geophysical Research*, 77(11), 2087–2103. <https://doi.org/10.1029/JB077i011p02087>
- Koketsu, K., & Sekine, S. (1998). Pseudo-bending method for three-dimensional seismic ray tracing in a spherical Earth with discontinuities. *Geophysical Journal International*, 132(2), 339–346. <https://doi.org/10.1046/j.1365-246x.1998.00427.x>
- Lay, T., Kanamori, H., & Ruff, L. (1982). The asperity model and the nature of large subduction zone earthquakes. *Earthquake Prediction Research*, 1, 3–72.
- Li, C., van der Hilst, R. D., Engdahl, E. R., & Burdick, S. (2008). A new global model for P wave speed variations in Earth's mantle. *Geochemistry, Geophysics, Geosystems*, 9, Q05018. <https://doi.org/10.1029/2007GC001806>
- Marcaillou, B., Collot, J. Y., Ribodetti, A., d'Acremont, E., Mahamat, A. A., & Alvarado, A. (2016). Seamount subduction at the North-Ecuadorian convergent margin: Effects on structures, inter-seismic coupling and seismogenesis. *Earth and Planetary Science Letters*, 433, 146–158. <https://doi.org/10.1016/j.epsl.2015.10.043>
- Mendoza, C., & Dewey, J. W. (1984). Seismicity associated with the great Colombia-Ecuador earthquakes of 1942, 1958, and 1979: Implications for barrier models of earthquake rupture. *Bulletin of the Seismological Society of America*, 74(2), 577–593.
- Moreno, M., Haberland, C., Oncken, O., Rietbrock, A., Angiboust, S., & Heidbach, O. (2014). Locking of the Chile subduction zone controlled by fluid pressure before the 2010 earthquake. *Nature Geoscience*, 7(4), 292–296. <https://doi.org/10.1038/ngeo2102>
- Mosegaard, K., & Tarantola, A. (1995). Monte Carlo sampling of solutions to inverse problems. *Journal of Geophysical Research*, 100(B7), 12,431–12,447. <https://doi.org/10.1029/94JB03097>
- Nocquet, J. M., Jarrin, P., Vallée, M., Mothes, P. A., Grandin, R., Rolandone, F., et al. (2017). Supercycle at the Ecuadorian subduction zone revealed after the 2016 Pedernales earthquake. *Nature Geoscience*, 10(2), 145–149. <https://doi.org/10.1038/ngeo2864>
- Nocquet, J. M., Villegas-Lanza, J. C., Chlieh, M., Mothes, P. A., Rolandone, F., Jarrin, P., et al. (2014). Motion of continental slivers and creeping subduction in the northern Andes. *Nature Geoscience*, 7(4), 287–291. <https://doi.org/10.1038/ngeo2099>
- Okada, Y. (1985). Surface deformation due to shear and tensile faults in a half-space. *Bulletin of the Seismological Society of America*, 75(4), 1135–1154.
- Pesicek, J. D., Thurber, C. H., Zhang, H., DeShon, H. R., Engdahl, E. R., & Widiyantoro, S. (2010). Teleseismic double-difference relocation of earthquakes along the Sumatra-Andaman subduction zone using a 3-D model. *Journal of Geophysical Research*, 115, B10303. <https://doi.org/10.1029/2010JB007443>
- Pesicek, J. D., Zhang, H., & Thurber, C. H. (2014). Multiscale seismic tomography and earthquake relocation incorporating differential time data: Application to the Maule subduction zone, Chile. *Bulletin of the Seismological Society of America*, 104(2), 1037–1044. <https://doi.org/10.1785/0120130121>
- Pontoise, B., & Monfret, T. (2004). Shallow seismogenic zone detected from an offshore-onshore temporary seismic network in the Esmeraldas area (northern Ecuador). *Geochemistry, Geophysics, Geosystems*, 5, 22. <https://doi.org/10.1029/2003GC000561>
- Reyes, C. G., & West, M. E. (2011). The waveform suite: A robust platform for manipulating waveforms in MATLAB. *Seismological Research Letters*, 82(1), 104–110. <https://doi.org/10.1785/gssrl.82.1.104>
- Rietbrock, A., & Waldhauser, F. (2004). A narrowly spaced double-seismic zone in the subducting Nazca plate. *Geophysical Research Letters*, 31, L10608. <https://doi.org/10.1029/2004GL019610>
- Rolandone, F., Nocquet, J.-M., Mothes, P. A., Jarrin, P., Vallée, M., Cubas, N., et al. (2018). Areas prone to slow slip events impede earthquake rupture propagation and promote afterslip. *Science Advances*, 4(1), ea06596. <https://doi.org/10.1126/sciadv.aao6596>
- Storchak, D. A., Bird, A. L., & Adams, R. D. (2000). Discrepancies in earthquake location between ISC and other agencies. *Journal of Seismology*, 4(3), 321–331. <https://doi.org/10.1023/A:1009815401999>
- Syracuse, E. M., & Abers, G. A. (2009). Systematic biases in subduction zone hypocenters. *Geophysical Research Letters*, 36, L10303. <https://doi.org/10.1029/2009GL037487>
- Um, J., & Thurber, C. (1987). A fast algorithm for two-point seismic ray tracing. *Bulletin of the Seismological Society of America*, 77(3), 972–986.
- Vaca, S., Vallée, M., Nocquet, J.-M., Battaglia, J., & Régnier, M. (2018). Recurrent slow slip events as a barrier to the northward rupture propagation of the 2016 Pedernales earthquake (Central Ecuador). *Tectonophysics*, 724–725, 80–92. <https://doi.org/10.1016/j.tecto.2017.12.012>
- Vallée, M., Nocquet, J. M., Battaglia, J., Font, Y., Segovia, M., Rengnier, M., & Chlieh, M. (2013). Intense interface seismicity triggered by a shallow slow slip event in the Central Ecuador subduction zone. *Journal of Geophysical Research: Solid Earth*, 118, 2965–2981. <http://doi.org/10.1002/jgrb.50216>
- Waldhauser, F., & Ellsworth, W. L. (2000). A double-difference earthquake location algorithm: Method and application to the northern Hayward fault, California. *Bulletin of the Seismological Society of America*, 90(6), 1353–1368. <https://doi.org/10.1785/0120000006>
- Waldhauser, F., & Schaff, D. (2007). Regional and teleseismic double-difference earthquake relocation using waveform cross-correlation and global bulletin data. *Journal of Geophysical Research*, 112, B12301. <https://doi.org/10.1029/2007JB004938>
- Waldhauser, F., & Schaff, D. P. (2008). Large-scale relocation of two decades of Northern California seismicity using cross-correlation and double-difference methods. *Journal of Geophysical Research*, 113, B08311. <https://doi.org/10.1029/2007JB005479>
- Wessel, P., & Smith, W. H. (1998). New, improved version of Generic Mapping Tools released. *Eos, Transactions American Geophysical Union*, 79(47), 579–579. <https://doi.org/10.1029/98EO00426>
- Weston, J., Ferreira, A. M., & Funning, G. J. (2012). Systematic comparisons of earthquake source models determined using InSAR and seismic data. *Tectonophysics*, 532–535, 61–81. <https://doi.org/10.1016/j.tecto.2012.02.001>
- Weston, J., Ferreira, A. M. G., & Funning, G. J. (2011). Global compilation of interferometric synthetic aperture radar earthquake source models: 1, Comparisons with seismic catalogs. *Journal of Geophysical Research*, 116, B08408. <https://doi.org/10.1029/2010JB008131>
- Wyss, M., Elashvili, M., Jorjashvili, N., & Javakhishvili, Z. (2011). Uncertainties in teleseismic earthquake locations: Implications for real-time loss estimates. *Bulletin of the Seismological Society of America*, 101(3), 1152–1161. <https://doi.org/10.1785/0120100168>
- Yagüe-Martínez, N., Prats-Iraola, P., González, F. R., Brcic, R., Shau, R., Geudtner, D., et al. (2016). Interferometric processing of Sentinel-1 TOPS data. *IEEE Transactions on Geoscience and Remote Sensing*, 54(4), 2220–2234. <https://doi.org/10.1109/TGRS.2015.2497902>
- Ye, L., Kanamori, H., Avouac, J. P., Li, L., Cheung, K. F., & Lay, T. (2016). The 16 April 2016, M W 7.8 (M S 7.5) Ecuador earthquake: A quasi-repeat of the 1942 M S 7.5 earthquake and partial re-rupture of the 1906 M S 8.6 Colombia–Ecuador earthquake. *Earth and Planetary Science Letters*, 454, 248–258. <https://doi.org/10.1016/j.epsl.2016.09.006>
- Yepes, H., Audin, L., Alvarado, A., Beauval, C., Aguilar, J., Font, Y., & Cotton, F. (2016). A new view for the geodynamics of Ecuador: Implication in seismogenic source definition and seismic hazard assessment. *Tectonics*, 35, 1249–1279. <https://doi.org/10.1002/2015TC003941>

- Yi, L., Xu, C., Wen, Y., Zhang, X., & Jiang, G. (2018). Rupture process of the 2016 Mw 7.8 Ecuador earthquake from joint inversion of InSAR data and teleseismic P waveforms. *Tectonophysics*, *722*, 163–174. <https://doi.org/10.1016/j.tecto.2017.10.028>
- Yoshimoto, M., Kumagai, H., Acero, W., Ponce, G., Vásconez, F., Arrais, S., et al. (2017). Depth-dependent rupture mode along the Ecuador-Colombia subduction zone. *Geophysical Research Letters*, *44*, 2203–2210. <https://doi.org/10.1002/2016GL071929>
- Yu, C., Li, Z., & Penna, N. T. (2017). Interferometric synthetic aperture radar atmospheric correction using a GPS-based iterative tropospheric decomposition model. *Remote Sensing of Environment*, *204*, 109–121. <https://doi.org/10.1016/j.rse.2017.10.038>
- Yu, C., Penna, N. T., & Li, Z. (2017). Generation of real-time mode high-resolution water vapor fields from GPS observations. *Journal of Geophysical Research: Atmospheres*, *122*, 2008–2025. <https://doi.org/10.1002/2016JD025753>
- Zhang, H., & Thurber, C. H. (2003). Double-difference tomography: The method and its application to the Hayward fault, California. *Bulletin of the Seismological Society of America*, *93*(5), 1875–1889. <https://doi.org/10.1785/0120020190>